High-pressure structure of praseodymium revisited: In search of a uniform structural phase sequence for the lanthanide elements

Citation for published version:
Finnegan, SE, Stevenson, MG, Pace, EJ, Storm, CV, McHardy, JD, McMahon, MI, MacLeod, SG, Plekhanov, E, Bonini, N & Weber, C 2022, 'High-pressure structure of praseodymium revisited: In search of a uniform structural phase sequence for the lanthanide elements', *Physical Review B*, vol. 105, no. 17, 174104, pp. 1-8. https://doi.org/10.1103/PhysRevB.105.174104

Digital Object Identifier (DOI):
10.1103/PhysRevB.105.174104

Published In:
Physical Review B

High-pressure structure of praseodymium revisited: In search of a uniform structural phase sequence for the lanthanide elements

S. E. Finnegan, M. G. Stevenson, E. J. Pace, C. V. Storm, J. D. McHardy, and M. I. McMahon
SUPA, School of Physics and Astronomy, and Centre for Science at Extreme Conditions, The University of Edinburgh, Peter Guthrie Tait Road, Edinburgh EH9 3FD, United Kingdom

S. G. MacLeod
AWE, Aldermaston, Reading RG7 4PR, United Kingdom and SUPA, School of Physics and Astronomy, and Centre for Science at Extreme Conditions, The University of Edinburgh, Peter Guthrie Tait Road, Edinburgh EH9 3FD, United Kingdom

E. Plekhanov, N. Bonini, and C. Weber
Theory and Simulation of Condensed Matter (TSCM), Department of Physics, King's College London, The Strand, London WC2R 2LS, United Kingdom

(Received 20 December 2021; revised 29 March 2022; accepted 26 April 2022; published 9 May 2022)

Angle-dispersive x-ray powder diffraction experiments have been performed on praseodymium metal to a pressure of 205 GPa. Between 20 and 165 GPa only the *oC*4 (α-uranium) phase is observed, in agreement with previous studies. At 171(5) GPa we find a transition to a tetragonal *tI*2 phase which is isostructural with the high-pressure post-*oC*4 phase seen in the neighboring lanthanide cerium above 12 GPa, and with the high-pressure phase of the actinide thorium seen above 100 GPa. Electronic structure calculations determine the *oC*4 $\rightarrow$ *tI*2 transition to occur at 130 GPa at 0 K, but find another phase, with the *hP*1 (simple hexagonal) structure, to have a lower enthalpy than both the *oC*4 and *tI*2 structures above 20 GPa at 0 K.

DOI: 10.1103/PhysRevB.105.174104

I. INTRODUCTION

On compression, the predominantly trivalent lanthanide metals (La to Lu, excluding Ce, Eu, and Yb) exhibit a common series of structural phase transformations: hcp (*hP*2 in Pearson notation) $\rightarrow$ Sm-type (*hR*9) $\rightarrow$ dhcp (*hP*4) $\rightarrow$ fcc (*cF*4) $\rightarrow$ distorted-fcc (*hR*24, *oI*16, or *oS*8) [1–3]. The pressures at which the transitions occur increase with increasing atomic number Z across the series [4].

Under further compression, the distorted-fcc structures undergo first-order volume collapse transitions into phases with more complex structures, typically with the hexagonal *hP*3 structure [5,6], the orthorhombic *oF*8 and *oF*16 structures [6–8], or the orthorhombic *oC*4 (α-uranium) structure [4,9–11]. The *oF*8 and *oC*4 structures are also seen in the actinide elements Pu and U, respectively, at ambient pressure [1], and also in Am, Cm, and Cf at high pressure [12–14].

Pr is the lowest-Z member of the trivalent lanthanides in which the *hP*4 $\rightarrow$ *cF*4 $\rightarrow$ *hR*24 $\rightarrow$ *oC*4 sequence of transitions is observed, with transition pressures of approximately 6, 7, and 20 GPa [2,4,10]. In Pr, an additional phase with an orthorhombic *oI*16 structure is seen between the *hR*24 and *oC*4 phases from 14 and 20 GPa [15]. *oC*4-Pr is then stable to 147(5) GPa, where it is reported to transform to an orthorhombic *oP*4 structure, different from both the tetragonal post-*oC*4 structure (*tI*2) reported in neighboring Ce [16] and the *oP*4 structure reported in Am, Cm, and Cf [12–14].

As the trivalent lanthanide metals are expected to continue exhibiting a common transition sequence at pressures higher than those at which they have been studied to date (typically 150–300 GPa), confirming the existence and structure of the *oP*4 phase in Pr is important, as it is currently seen only in that element.

In order to confirm the structure of the post-*oC*4 phase in Pr, we have conducted x-ray diffraction studies from 65 to 205 GPa. In contrast to the previous study, we find the structure of the post-*oC*4 phase of Pr to be *tI*2, the same as that seen in Ce above 13 GPa [16–18], in Th above 100 GPa [19,20], and calculated to be the structure of the post-*oC*4 phase in U itself above ~800 GPa [21], suggesting that this is the next common structure in the trivalent lanthanide transition sequence.

II. EXPERIMENTAL DETAILS

High-purity distilled samples of commercially purchased Pr, supplied by Ulrich Schwarz of the Max-Planck-Institut für Chemische Physik fester Stoffe in Dresden, were loaded into two DACs in a dry argon atmosphere (<0.1 ppm O_2 and <0.1 ppm H_2O) to prevent oxidation. The measured impurity levels in the supplied samples were oxygen $< 0.05(2)\%$, nitrogen $= 0.033(4)\%$, and carbon $< 0.06\%$. The Pr was highly crystalline, as determined by the sharp diffraction peaks from the as-loaded samples, and in contrast to our previous study

[15] we observed no diffraction peaks from oxide or hydride contaminants as a result of the loading process.

The DACs were equipped with beveled diamonds, one with 100 μm diameter culets (sample 1) and the other with 50 μm diameter culets (sample 2), and W gaskets. The samples were loaded without any pressure-transmitting medium (PTM) so as to prevent contamination. Both samples were loaded with several small (a few μm) copper (Cu) spheres to act as a pressure calibrant, using the published Cu equation of state (EOS) of Sokolova *et al.* [22].

Diffraction data were collected in two experiments on the Extreme Conditions P02.2 beamline at the PETRA III synchrotron in Hamburg, Germany. Additional lower-pressure data up to 23 GPa were obtained in 2008 on beamline 9.5HPT at the now-closed Synchrotron Radiation Source (SRS) at Daresbury Laboratory in the UK [15,23]. Monochromatic x-ray beams of wavelength 0.4832 Å (PETRA III) and 0.4438 Å (SRS), focused down to a FWHM of 0.85 μm $\times$ 0.85 μm (PETRA III) [6] and 50 μm $\times$ 50 μm (SRS), were used, and the powder-diffraction data were recorded on Perkin-Elmer (PETRA III) and Mar345 (SRS) area detectors, placed 300–400 mm from the sample. LaB_6 and CeO_2 diffraction standards were used to calibrate the exact sample-detector distance and the detector tilts in each experiment. The 2D diffraction images collected at each pressure were integrated azimuthally using DIOPTAS [24] or FIT2D [25] to obtain standard 1D diffraction profiles, which were then analyzed using Rietveld [26] and Le Bail profile-fitting methods, or by fitting to the measured d spacings of individual diffraction peaks [27].

The absence of a PTM can result in significant pressure gradients within the sample. The submicron beam available at PETRA III enabled us to map the pressure distribution over the central 10 μm $\times$ 10 μm area in both sample 1 and 2 at 174 GPa and 193 GPa, respectively, and the results are shown in Figs. 1 and 2. Despite the presence of pressure variations of 6 and 11 GPa, respectively, in the 10 μm $\times$ 10 μm sample areas over which the pressure distribution was measured, the pressure variation within the 0.85 μm $\times$ 0.85 μm area sampled by the x-ray beam was negligible in each case.

The absence of measurable pressure gradients or anisotropic stress in the sample was also evident in the diffraction profiles, which exhibited only very slight azimuthal variations in 2θ around each Debye-Scherrer ring, resulting in excellent Rietveld fits to the diffraction profiles to the highest pressures (see next section).

III. RESULTS AND DISCUSSION

As the low-pressure phases of Pr have been well studied, and the *oC*4 phase is known to exist from 20 GPa up to ~150 GPa, no diffraction data were collected from samples 1 and 2 below 65 GPa. Profile-fitting of the diffraction data collected from 65 to 165 GPa showed that the *oC*4 structure is stable up to this pressure. Figure 3 shows a Rietveld refinement of this structure to a diffraction profile from Pr at 165 GPa—the highest pressure at which single-phase profiles of *oC*4-Pr were obtained. The refined lattice parameters at this pressure are $a = 2.4199(4)$ Å, $b = 4.7817(5)$ Å, and $c = 4.3799(7)$ Å, $V/V_0 = 0.366(1)$, with atoms on the 4c Wyckoff site at (0, 0.115(17), $\frac{1}{4}$). The fit is excellent, with all of the observed diffraction peaks accounted for. The remaining intensity misfits arise from the textured nature of the Debye-Scherrer rings.

On further compression above 165 GPa, clear changes were observed in the diffraction profiles, as illustrated in Fig. 4. Above this pressure, diffraction peaks from *oC*4-Pr

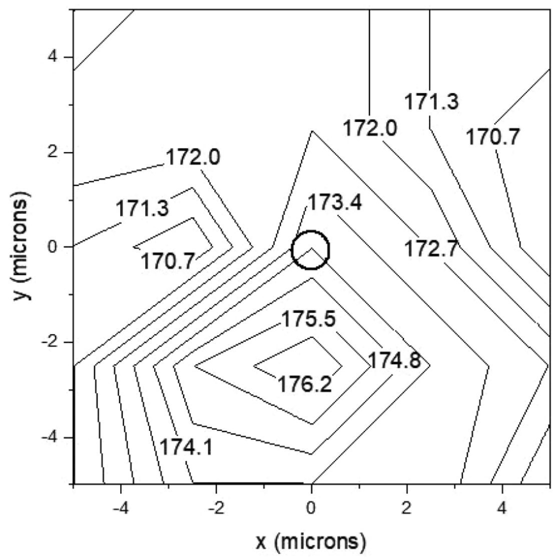

FIG. 1. The pressure distribution over the central 10 μm $\times$ 10 μm area of sample 1 at 174 GPa. Also shown for comparison is the 0.85 μm x-ray beam diameter (FWHM) used to obtain the diffraction data at PETRA III. Despite a pressure gradient of 6 GPa within the mapped region, the pressure variation within the sample volume probed by the 0.85 μm diameter beam is negligible.

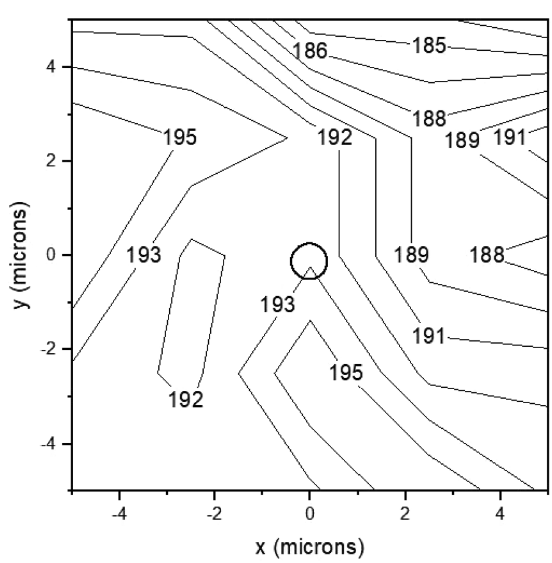

FIG. 2. The pressure distribution over the central 10 μm $\times$ 10 μm area of sample 2 at 193 GPa. Also shown for comparison is the 0.85 μm x-ray beam diameter used to obtain the diffraction data at PETRA III. Despite a pressure gradient of 11 GPa within the mapped region, the pressure variation within the sample volume probed by the 0.85 μm diameter beam is negligible.

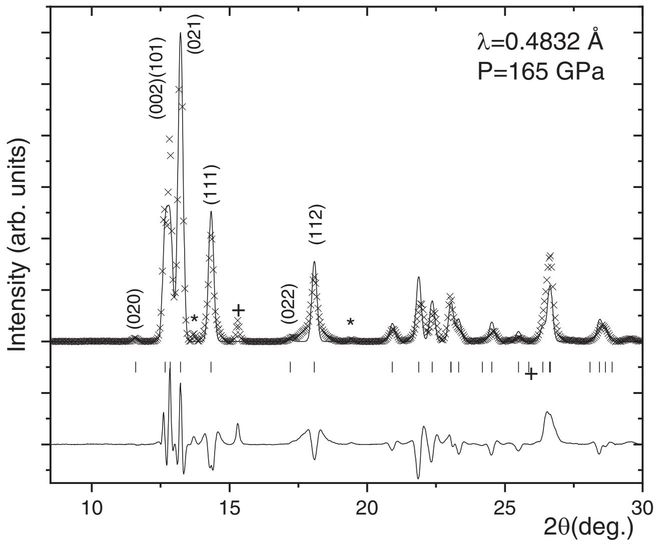

FIG. 3. Rietveld refinement of the *oC*4 structure to a background-subtracted diffraction profile from Pr at 165 GPa, showing the observed (crosses) and calculated (line) diffraction patterns, the calculated reflection positions, and the difference profile [$R_P = 3.5\%$, $R_{wP} = 5.8\%$, GoF = 1.19, $R(F^2) = 16.6\%$, and preferred orientation in the (021) direction]. The first seven peaks of the *oC*4 phase are labeled with their Miller indices. The asterisks identify weak peaks from the W gasket, and the + symbol identifies a peak from the Cu pressure calibrant.

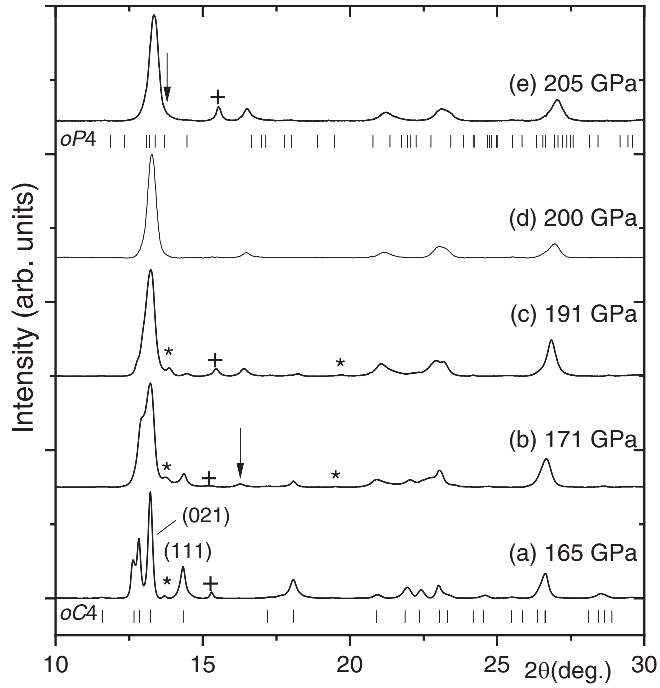

FIG. 4. Background-subtracted diffraction profiles collected from Pr on pressure increase from 165 GPa to 205 GPa. The data were collected from the two samples at PETRA III using $\lambda = 0.4832$ Å. Tick marks beneath profile (a) show the best-fitting peak positions for the *oC*4 phase at this pressure (as obtained from Fig. 3), while the tick marks beneath profile (e) show the calculated peak positions for the reported *oP*4 structure at 205 GPa, assuming lattice parameters of $a = 2.380$ Å, $b = 4.673$ Å, and $c = 4.499$ Å. The peak marked with an arrow in profile (b) is the most evident new peak from the post-*oC*4 phase, while the arrow in profile (e) identifies the (012) peak of the *oP*4 structure, which we do not observe. The peaks marked with asterisks in profiles (a)–(c) are from the W gasket, while peaks marked with + are from the Cu pressure marker. Profiles (a)–(c) were obtained from sample 1, in which the diamonds failed at 191 GPa, and profiles (d) and (e) were obtained from sample 2.

decreased in intensity while peaks from the post-*oC*4 phase became more intense [see Figs. 4(b) and 4(c)], with the result that the diffraction pattern simplified. Above 200 GPa no further changes were observed in the diffraction profiles, suggesting that single-phase profiles of the post-*oC*4 phase were observed above this pressure [Figs. 4(d) and 4(e)].

Velisavljevic and Vohra [28] previously reported a transition in the *oC*4 phase at 147(5) GPa, as determined by the appearance of a new diffraction peak between the (021) and the (111) peaks of the *oC*4 phase [indexed in Fig. 4(a)] which, unusually, moved to *longer d* spacing with increased pressure. However, comparison of Fig. 1 in Ref. [28] with Fig. 4 shows that we see no new peak at that location.

The tick marks beneath Fig. 4(e) show the expected peak positions from the *oP*4 structure reported by Velisavljevic and Vohra at 205 GPa, using estimated lattice parameters at this pressure ($a = 2.380$ Å, $b = 4.673$ Å, and $c = 4.499$ Å), as determined from Fig. 4 in Ref. [28]. It is clear that while a number of the tick marks align with observed peaks in the diffraction profile, many of the peaks predicted by the *oP*4 structure are not observed. In particular, the peak at 13.7° [identified with an arrow in profile (e) of Fig. 4], which indexes as the (012) in the *oP*4 structure, and the appearance of which was a key indicator of the transition to the post-*oC*4 phase in the study of Velisavljevic and Vohra, is not observed in any of our diffraction profiles.

As said, the diffraction profiles we observed from the post-*oC*4 phase were simpler than those from the *oC*4 phase itself, suggesting they came from a structure with higher symmetry and/or with a smaller unit cell. Previous studies of the high-pressure behavior of Ce have reported similar simplifications of the diffraction profiles at the *oC*4 → *tI*2 transition [16,18,30,31], and comparisons of the diffraction profiles from *tI*2-Ce [16,31,32] with those observed in Pr above 200 GPa [Figs. 4(d) and 4(e)] showed them to be similar.

Figure 5 shows a Rietveld fit of the tetragonal *tI*2 structure to the background-subtracted diffraction profile from Pr at 205(3) GPa. The refined lattice parameters are $a = 2.383(4)$ Å and $c = 4.209(11)$ Å, $V/V_0 = 0.342(1)$, with atoms on the 2*a* site of space group $I4/mmm$ at (000). The fit is excellent, with all of the observed diffraction peaks from the sample being accounted for.

The compressibility of Pr to 205 GPa is shown in Fig. 6. At low pressures, while undergoing the *hP*4 → *cF*4 → *hR*24 transition sequence, the compressibility of Pr is very similar to that of Sm and Nd over the same pressure range [6,7]. However, at 14 and 20 GPa, Pr undergoes two first-order transitions to the *oI*16 and *oC*4 phases, with volume decreases ($\Delta V/V_0$) of ∼0% and 6.2(1)%, respectively [15], after which the compressibility of Pr is considerably lower. At 171 GPa,

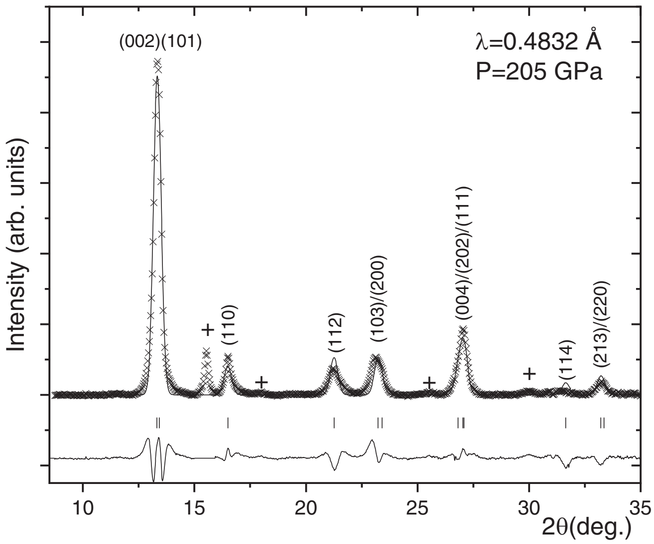

FIG. 5. Rietveld refinement of the $tI2$ structure to a background-subtracted diffraction profile from Pr at 205 GPa, showing the observed (crosses) and calculated (line) diffraction patterns, the calculated reflection positions, and the difference profile [$R_P = 0.9\%$, $R_{wP} = 1.7\%$, GoF = 0.5, $R(F^2) = 5.2\%$, preferred orientation in the (120) direction]. All of the peaks from the $tI2$ phase are labeled with their Miller indices, while peaks marked with + symbols are from the Cu pressure calibrant.

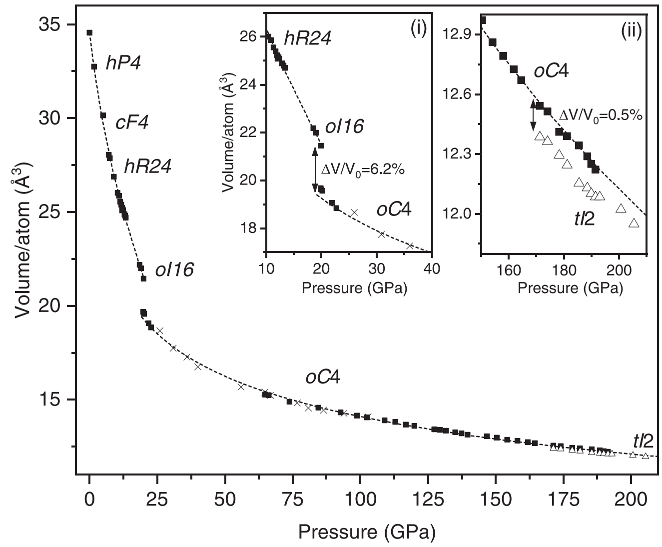

FIG. 6. The compressibility of Pr to 205 GPa. The data from our previous measurements to 22 GPa [15] and the current study of $oC4$-Pr from 65 to 192 GPa are plotted with solid symbols, while the data for $oC4$-Pr from the study of Chesnut and Vohra [29] are shown as crosses. The current data on $tI2$-Pr are shown with unfilled triangles to distinguish them from $oC4$-Pr. Inset (i) highlights the volume change of ~6% at the $oI16 \rightarrow oC4$ transition, while inset (ii) highlights the volume change of ~0.5% at the $oC4 \rightarrow tI2$ transition. The dashed lines through the data points are the AP2 EOS fits.

the first-order transition to $tI2$-Pr results in a further ~0.5% ($\Delta V/V_0$) in volume, with the compressibility of $tI2$-Pr being similar to that of $oC4$-Pr at the same pressures [see inset (ii) to Fig. 6].

To identify and analyze the changes in compression data of the trivalent lanthanides, we have previously utilized Holzapfel's Adapted Polynomial of order L (APL) EOS formalism to analyze their compressibilities [33]. This EOS has several advantages over other formalisms, and enables the compressibility to be linearized straightforwardly. Nonlinear behavior can then be interpreted as arising from deviations from the regular compressive behavior expected for a normal metal, perhaps arising from changes in the electronic structure [34].

If one fits the compression data using the second-order (AP2) form of the APL EOS [33,35],

$$P = 3K_0 \frac{(1-x)}{x^5} \exp[c_0(1-x)][1 + xc_2(1-x)], \quad (1)$$

where K_0 is the zero-pressure bulk modulus, K' is its pressure derivative, $x = (V/V_0)^{1/3}$, $c_0 = -\ln(3K_0/p_{\mathrm{FG}})$, $c_2 = (3/2)(K'-3) - c_0$, $p_{\mathrm{FG}} = a_{\mathrm{FG}}(Z/V_0)^{5/3}$ is the Fermi-gas pressure, Z is the atomic number, and $a_{\mathrm{FG}} = [(3\pi^2)/5](\hbar^2/m_e) = 0.02337$ GPa nm^5 is a constant, then the compression data can be linearized in a so-called η_{APL}-x plot:

$$\eta_{\mathrm{APL}}(x) = \ln\left(\frac{px^5}{p_{\mathrm{FG}}}\right) - \ln(1-x). \quad (2)$$

In this work, in order to better realize differences in behavior to "regular" compressive behavior, described below, it is convenient to transform this linearization into σ space, where $\sigma = \sigma_0 x$ and σ_0 is the Thomas-Fermi radius $(3ZV_0/4\pi)^{1/3}$.

Figure 7 shows the APL linearized compression data for Pr in the form of an η_{APL}-σ plot. In such a plot, materials undergoing regular compression will show linear or quasilinear behavior, with a negative gradient, and the correct theoretical limit of $\eta(0) = 0$. While the data for Pr exhibit linear behavior at low pressures, the gradient is positive, and similar to that we have observed recently in Nd and Sm [6,7]. The positive gradient indicates that the $hP4$, $cF4$, $hR24$, and $oI16$ phases of Pr are more compressible than would be expected from its ambient pressure atomic volume and its atomic number. Such deviations from regular compressive behavior expected from a normal metal can arise from changes in electronic structure [34].

However, Fig. 7 shows that there is a striking change in compressive behavior after Pr undergoes the first-order phase transition to the $oC4$ phase at 20 GPa ($\sigma \sim 6.6$ Å), after which the linearized data from both the $oC4$ and $tI2$ phases show the negative gradient of a regular metal with the correct limiting behavior of $\eta(0) \sim 0$.

The distinct change in compression seen after the d-$cF4 \rightarrow oC4$ transition in Pr at 20 GPa is much more dramatic than that seen in Nd or Sm, where the change to "regular" behavior takes place more gradually, over multiple phases [6,7]. However, in Pr, the $oI16 \rightarrow oC4$ transition occurs via a sizable volume change ($\Delta V/V_0$) of 6% [see inset (i) to Fig. 6], much larger than the 0.4% volume change seen at the $hP4 \rightarrow oF8$ and $oF8 \rightarrow oC4$ transitions in Nd, and volume changes in Sm that were too small to measure [6,7]. Above the $oI16 \rightarrow oC4$ transition at 20 GPa, in both the $oC4$ and

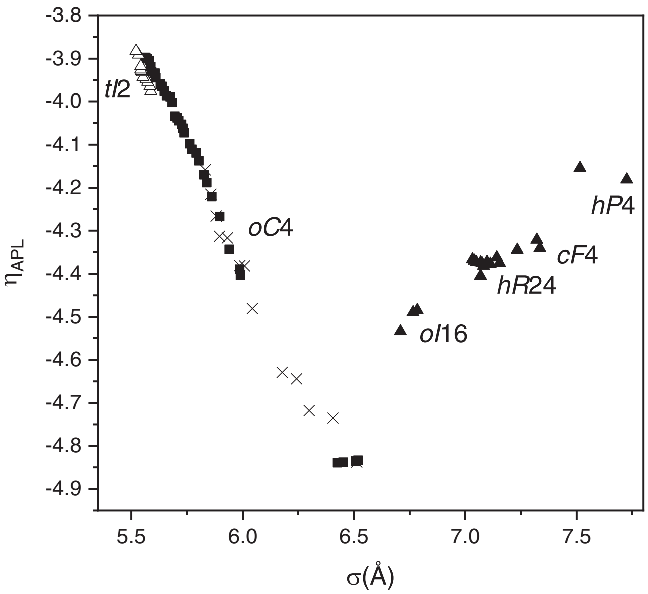

FIG. 7. Linearization of the compression of Pr shown in the form of an η_{APL}-σ plot, where $\sigma = \sigma_0 x$. The data from the lower-pressure phases (*hP*4, *cF*4, *hR*24, and *oI*16) are plotted with filled triangles, while our data from *oC*4-Pr are plotted with filled squares and the *oC*4-Pr data from the study of Chesnut and Vohra [29] are shown as crosses. For clarity, the current data for *tI*2-Pr are plotted with unfilled triangles.

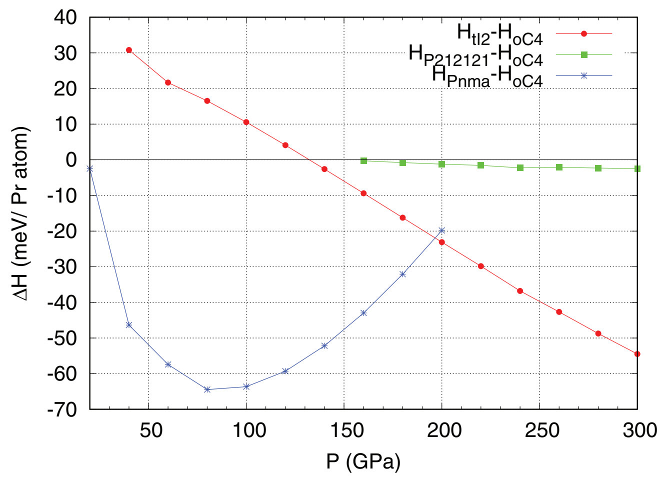

FIG. 8. The enthalpies of the *tI*2-Pr, $P2_12_12_1$-Pr, and *Pnma*-Pr relative to that of *oC*4-Pr from 20 to 300 GPa. *tI*2-Pr becomes significantly more stable than *oC*4-Pr at pressures above 130 GPa. Also shown is the enthalpy curve for the second *Pnma* structure, the true structure of which is simple hexagonal, *hP*1.

*tI*2 phases, Pr shows the same regular compressive behavior (Fig. 7), with a very similar gradient to that seen in both *oF*8-Nd and *oC*4-Nd above 71 GPa, and in *oF*8-Sm above 93 GPa.

IV. ELECTRONIC STRUCTURE CALCULATIONS

To gain further insight and understanding into the behavior of Pr at high compression, we have performed DFT calculations of the *oC*4 and *tI*2 structures of Pr, as well as the *oP*4 structure (space group $P2_12_12_1$) reported by Velisavljevic [28] in Pr, and the different *oP*4 structure (space group *Pnma*) previously reported in Am, Cm, and Cf [12–14]. Structural optimization of bulk Pr in each phase was accomplished by using DFT calculations with the VASP [36] package, utilizing the Perdew-Burke-Ernzerhof functional [37]. The *k*-point sampling was performed using Monkhorst-Pack meshes, ensuring a *k*-point density of at least 0.1 Å^{-1} for all the structures at 40 GPa, while a Gaussian smearing of 0.1 eV was used. During the DFT structural optimization, a convergence on internal forces and stress tensor of 0.01 eV/Å was reached, and the energy cutoff was set to 500 eV. Scalar relativistic spin-orbit coupling was taken into account within the Koelling-Harmon approximation [38].

Our zero-temperature DFT calculations revealed that *tI*2-Pr becomes lower in enthalpy than the *oC*4-Pr at pressures above $P = 130$ GPa, in agreement with the experimental findings, while we found that the *oP*4 ($P2_12_12_1$) structure at high pressure ($P \geqslant 150$ GPa) is very close in enthalpy to the *oC*4 phase, but much higher in enthalpy than the *tI*2 phase. These results, which are illustrated in Fig. 8, allow us to exclude with confidence the presence of this *oP*4 structure in Pr at high pressure.

The enthalpy gain of *tI*2-Pr over *oC*4-Pr above 130 GPa is dominated by the *PV* term, yielding the linear dependence on pressure evident in Fig. 8, so that the *tI*2 phase eventually wins because of more compact Pr atomic arrangement. The theoretically estimated zero-temperature transition pressure of 130 GPa is somewhat lower than the transition pressure of 171 GPa observed experimentally at room temperature. In all the structures studied, Pr appears to have no net magnetic moment, as previously seen experimentally at low pressure in Ref. [39], and in contrast to the magnetic behavior we have seen in Sm and Nd [6,7].

Surprisingly, our DFT calculations found *two* versions of the *oP*4 structure with space group *Pnma* with very different structural parameters. For example, at 160 GPa, we found one *Pnma* structure with $a = 4.7240$ Å, $b = 4.3730$ Å, and $c = 2.4084$ Å, with atoms on the 4*c* site at (0.1102, $\frac{1}{4}$, 0), and a second considerably lower enthalpy structure with $a = 4.7274$ Å, $b = 4.2832$ Å, $c = 2.4735$ Å, with atoms on 4*c* at (0, $\frac{1}{4}$, $\frac{1}{2}$). While the first of these structures is identical to the *oC*4 structure (space group *Pnma* is a subgroup of *Cmcm*, the space group of *oC*4), we note that in the second structure the b/c ratio is almost exactly $\sqrt{3}$, and this was also the case at all pressures when the same structure was optimized in 20 GPa increments between 40 and 200 GPa. This suggests that the true symmetry of the structure is hexagonal, and further analysis revealed that the correct space group is $P6/mmm$ with $a = 2.4735$ Å, $c = 2.3637$ Å and an atom at (0,0,0). This is the simple hexagonal structure, *hP*1 in Pearson notation, seen only in Si, Ge at high pressure, although the c/a ratios in these *hP*1 structures are slightly different (∼0.93 in Si and Ge [40,41]) from the calculated value of 0.96 in Pr.

The *hP*1 structure comprises close-packed hexagonal layers stacked directly above one another. In the *ABC* nomenclature used to describe the stacking of such layers, the stacking sequence is *AAA*. This then is the newest member of the family of high-pressure lanthanide structures comprising the stacking of hcp or quasi-hcp layers. Surprisingly, given that this structure has not been observed experimentally in elements other than in Si and Ge, our calculations show that *hP*1-Pr has the lowest enthalpy of all the Pr structures investigated between 20 and 200 GPa (see Fig. 8). Phonon calculations in *hP*1-Pr at 80 GPa, where it has the largest enthalpy offset from all the other phases tested, revealed no imaginary phonon modes, and therefore that the structure is dynamically stable.

Given the absence of any evidence of the *hP*1 structure in our diffraction data, we also investigated the magnetic ordering in each of the structures considered, differences which might alter their relative enthalpies. All the structures of Pr examined exhibited no net magnetic moment or antiferromagnetic order within DFT. Antiferromagnetism has previously been reported in Pr at ambient pressure and low temperatures [42], and theoretical modeling has described how magnetic order could arise in rare earth elements as a result of interaction between the localized moments and free conducting electrons [43] (Kondo model) or the Ruderman-Kittel-Kasuya-Yosida (RKKY) exchange mechanism [44], clearly indicating that a treatment beyond DFT would be needed to reproduce such behavior.

As our DFT calculations were performed at zero temperature, it remains possible that *hP*1-Pr is the stable structure between 20 and 200 GPa, but only at low temperatures. A density functional theory + dynamical mean field theory (DFT+DMFT) [45,46] study of Pr structures and magnetism, which correctly treats the electronic correlations at finite temperature, is in progress, and its results will be reported elsewhere. While there have been no low-temperature diffraction studies of Pr to date, the study of Tateiwa *et al.* [47] reported anomalies in the resistivity at ∼225 K above 20 GPa, perhaps suggesting the existence of a new phase below that temperature. Diffraction studies under the same *P-T* conditions are now needed to determine whether this is the case. The existence of a low-temperature structure that does not have the *oC*4 structure will be important for interpreting previous low-temperature resistivity and superconductivity measurements [48,49].

In light of our observation of the *tI*2 structure in Pr, we have revisited our previous calculations regarding the highest-pressure phases in Tb and Nd to determine at which pressure each element might also transform to the same structure. In Tb, the highest-pressure known phase has the *oF*16 structure, which is found to be stable above 60 GPa [8]. Extending our previous DFT calculations to higher pressures, and including both the *oC*4 and *tI*2 structures, we find that *oC*4 becomes more stable than *oF*16-Tb above 300 GPa, as shown in Fig. 9. On the other hand, *tI*2-Tb always remains much higher in enthalpy in comparison to both *oC*4-Tb and *oF*16-Tb. In all three structures, Tb has a comparable magnetic moment of between 5.5 and 4.7 μ_B/atom in the range of pressure between 40 and 400 GPa.

In Nd, we have previously reported that the *oC*4 phase is stable from 98 GPa to at least 302 GPa, the highest pressure to which it has been studied [7]. DFT calculations to higher pressures, and including the *tI*2 structure, show that the latter is always higher in enthalpy with respect to *oC*4-Nd phase, as

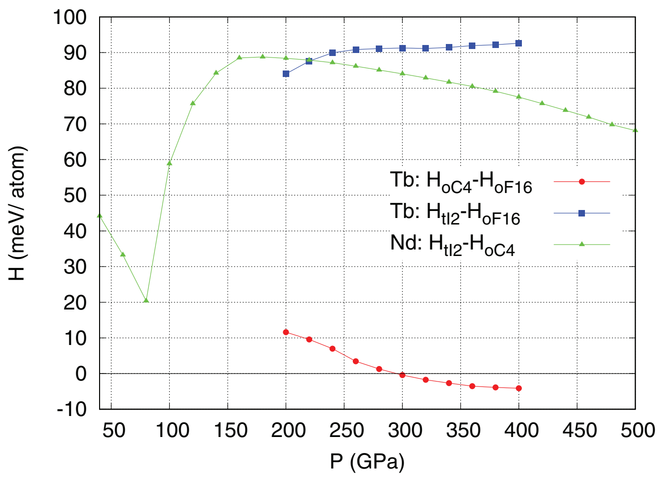

FIG. 9. The enthalpy gain per atom of *oC*4-Tb (red line) and *tI*2-Tb (blue line) relative to that of *oF*16-Tb. The *oC*4 phase becomes more stable than *oF*16 at pressures above approximately 300 GPa. However, the enthalpy of *tI*2-Tb is always significantly above those of the other two phases. Also shown is the enthalpy gain per atom of *tI*2-Nd relative to *oC*4-Nd (green line) from 40 to 500 GPa. The *oC*4 phase remains the most stable of the two over the whole range examined. The kink at 80 GPa is associated with the loss of magnetization in *oC*4-Nd at this pressure.

shown in Fig. 9. The kink at 80 GPa is associated with the loss of magnetization in the *oC*4 phase, while the broad maximum at $P = 160$ GPa is due to the loss of magnetization in the *tI*2 phase. Above 160 GPa, the enthalpy difference between *oC*4-Nd and *tI*2-Nd decreases monotonically, although remaining sizable (68 meV/atom) up to the maximum pressure of 500 GPa examined in the current work.

V. CONCLUSIONS

The post-*oC*4 phase of Pr stable above 171 GPa has been determined by x-ray diffraction to have a body-centred tetragonal structure with 2 atoms in the unit cell (Pearson symbol *tI*2) contrary to that which has been published previously [28]. The post-*oC*4 phase of neighboring lanthanide Ce is known to have the same *tI*2 structure up to 208 GPa [16–18], see Fig. 10, while the post-*oC*4 phase of U itself is calculated to have the *tI*2 structure above 800 GPa [21]. Measurements of the compressibility of Pr reveal that it becomes considerably less compressible after the transition to the *oC*4 phase at 20 GPa, and that in the *oC*4 and *tI*2 phases its compressibility is that expected of a regular metal.

Our DFT calculations reveal that *tI*2-Pr has a lower enthalpy than *oC*4-Pr above 130 GPa, in agreement with the experimental findings. However, the same calculations reveal that a simple hexagonal structure (*hP*1) has a considerably lower enthalpy than both the *oC*4 and *tI*2 phases between 20 and 200 GPa. However, we have observed no such phase in our room temperature diffraction study. Further calculations of the structural and magnetic behavior of Pr above 0 K are ongoing and will be published elsewhere.

Finally, given that the post-*oC*4 phases of both Ce and Pr have the *tI*2 structure, we have used DFT both to predict

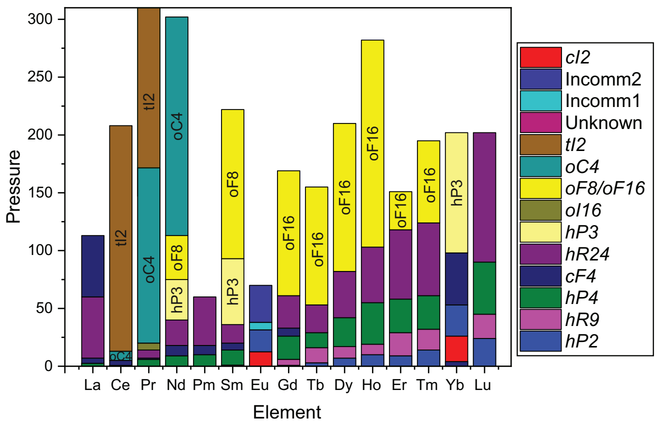

FIG. 10. The different phases reported in the lanthanide elements up to 310 GPa at ambient temperature, including the current results in Pr. With the exception of Ce, Eu, and Yb, the elements adopt a similar phase transition sequence, with the transition pressures increasing with increasing Z. The observation of the $tI2$ structure in Pr above 170 GPa strengthens the systematics between the different lanthanides, and suggests that this is the next common structure in the phase transition sequence. The phases are labeled using Pearson notations except for the two incommensurate phases of Eu which are denoted Incomm1 and Incomm2 [50,51].

the $oC4 \rightarrow tI2$ transition pressure in Nd and to determine at what pressure the same two structures might be observed in Tb. We find $tI2$-Nd to have a considerably higher enthalpy than $oC4$-Nd at all pressures up to 500 GPa, and probably to considerably higher. We estimate that $oF16$-Tb will transform to $oC4$-Tb at 300 GPa, but that the enthalpy of $tI2$-Nd remains well above that of $oC4$-Nd to well above 400 GPa. Whether the post-$oC4$ phase has the $tI2$ structure across the lanthanide elements is thus still unclear.

ACKNOWLEDGMENTS

British Crown Owned Copyright 2022/AWE. Published with permission of the Controller of Her Britannic Majesty's Stationery Office. This work was supported by grants (Grants No. EP/R02927X/1 and No. EP/R02992X/1) from the U.K. Engineering and Physical Sciences Research Council (EPSRC). We also acknowledge DESY (Hamburg, Germany), a member of the Helmholtz Association HGF, for the provision of experimental facilities. The research leading to this result has been supported by the project CALIPSOplus under Grant Agreement No. 730872 from the EU Framework Programme for Research and Innovation HORIZON 2020. We would like to thank H-P. Liermann, K. Glazyrin, and R. Husband for their assistance on the ECB beamline at PETRA III, and A. Lennie for his help at the 9.5HPT beamline at SRS. S.E.F., C.V.S., and J.D.M. are grateful to AWE for support through CASE studentships.

[1] D. A. Young, *Phase Diagrams of the Elements* (University of California Press, Oakland, 1991).
[2] N. Hamaya, Y. Sakamoto, H. Fujihisa, Y. Fujii, K. Takemura, T. Kikegawa, and O. Shimomura, J. Phys.: Condens. Matter **5**, L369 (1993).
[3] Y. R. Shen, R. S. Kumar, A. L. Cornelius, and M. F. Nicol, Phys. Rev. B **75**, 064109 (2007).
[4] T. Kruger, B. Merkau, W. A. Grosshans, and W. B. Holzapfel, High Press. Res. **2**, 193 (1990).
[5] R. J. Husband, I. Loa, K. A. Munro, and M. I. McMahon, J. Phys.: Conf. Ser. **500**, 032009 (2014).
[6] S. E. Finnegan, E. J. Pace, C. V. Storm, M. I. McMahon, S. G. MacLeod, H.-P. Liermann, and K. Glazyrin, Phys. Rev. B **101**, 174109 (2020).
[7] S. E. Finnegan, C. V. Storm, E. J. Pace, M. I. McMahon, S. G. MacLeod, E. Plekhanov, N. Bonini, and C. Weber, Phys. Rev. B **103**, 134117 (2021).
[8] M. I. McMahon, S. Finnegan, R. J. Husband, K. A. Munro, E. Plekhanov, N. Bonini, C. Weber, M. Hanfland, U. Schwarz, and S. G. Macleod, Phys. Rev. B **100**, 024107 (2019).
[9] M. I. McMahon and R. J. Nelmes, Phys. Rev. Lett. **78**, 3884 (1997).
[10] G. S. Smith and J. Akella, J. Appl. Phys. **53**, 9212 (1982).
[11] W. A. Grosshans, Y. K. Vohra, and W. B. Holzapfel, J. Phys. F **13**, L147 (1983).
[12] S. Heathman, R. G. Haire, T. Le Bihan, A. Lindbaum, K. Litfin, Y. Méresse, and H. Libotte, Phys. Rev. Lett. **85**, 2961 (2000).
[13] S. Heathman, R. G. Haire, T. Le Bihan, A. Lindbaum, M. Idiri, P. Normile, S. Li, R. Ahuja, B. Johansson, and G. H. Lander, Science **309**, 110 (2005).
[14] S. Heathman, T. Le Bihan, S. Yagoubi, B. Johansson, and R. Ahuja, Phys. Rev. B **87**, 214111 (2013).
[15] S. R. Evans, I. Loa, L. F. Lundegaard, and M. I. McMahon, Phys. Rev. B **80**, 134105 (2009).
[16] S. Endo, H. Sasaki, and T. Mitsui, J. Phys. Soc. Jpn. **42**, 882 (1977).
[17] Y. Zhao and W. B. Holzapfel, J. Alloys Compd. **246**, 216 (1997).
[18] Y. K. Vohra, S. L. Beaver, J. Akella, C. A. Ruddle, and S. T. Weir, J. Appl. Phys. **85**, 2451 (1999).
[19] Y. K. Vohra and J. Akella, Phys. Rev. Lett. **67**, 3563 (1991).
[20] Y. K. Vohra, Phys. B: Condens. Matter **190**, 1 (1993).
[21] P. Söderlind, O. Eriksson, B. Johansson, J. M. Wills, and A. M. Boring, Nature (London) **374**, 524 (1995).
[22] T. S. Sokolova, P. I. Dorogokupets, A. M. Dymshits, B. S. Danilov, and K. D. Litasov, Comput. Geosci. **94**, 162 (2016).
[23] S. R. Evans, High-pressure x-ray diffraction studies of light lanthanides, Ph.D. thesis, University of Edinburgh, 2010.
[24] C. Prescher and V. B. Prakapenka, High Press. Res. **35**, 223 (2015).
[25] A. P. Hammersley, S. O. Svensson, M. Hanfland, A. N. Fitch, and D. Hausermann, High Press. Res. **14**, 235 (1996).
[26] V. Petvříček, M. Dušek, and L. Palatinus, Z. Kristallogr. - Cryst. Mater. **229**, 345 (2014).

[27] T. J. B. Holland and S. A. T. Redfern, Mineral. Mag. **61**, 65 (1997).
[28] N. Velisavljevic and Y. K. Vohra, High Press. Res. **24**, 295 (2004).
[29] G. N. Chesnut and Y. K. Vohra, Phys. Rev. B **62**, 2965 (2000).
[30] G. Gu, Y. K. Vohra, and K. E. Brister, Phys. Rev. B **52**, 9107 (1995).
[31] K. A. Munro, D. Daisenberger, S. G. MacLeod, S. McGuire, I. Loa, C. Popescu, P. Botella, D. Errandonea, and M. I. McMahon, J. Phys.: Condens. Matter **32**, 335401 (2020).
[32] J. S. Olsen, S. Steenstrup, and L. Gerward, Phys. Lett. A **109**, 235 (1985).
[33] W. B. Holzapfel, High Press. Res. **16**, 81 (1998).
[34] W. B. Holzapfel, in *Correlations in Condensed Matter under Extreme Conditions* (Springer, Berlin, Heidelberg, 2017), pp. 91–106.
[35] W. B. Holzapfel, Z. Kristallogr. **216**, 473 (2001).
[36] G. Kresse and D. Joubert, Phys. Rev. B **59**, 1758 (1999).
[37] J. P. Perdew, K. Burke, and M. Ernzerhof, Phys. Rev. Lett. **77**, 3865 (1996).
[38] D. D. Koelling and B. N. Harmon, J. Phys. C **10**, 3107 (1977).
[39] H. Nagasawa and T. Sugawara, J. Phys. Soc. Jpn. **23**, 701 (1967).
[40] M. I. McMahon and R. J. Nelmes, Phys. Rev. B **47**, 8337 (1993).
[41] Y. K. Vohra, K. E. Brister, S. Desgreniers, A. L. Ruoff, K. J. Chang, and M. L. Cohen, Phys. Rev. Lett. **56**, 1944 (1986).
[42] J. W. Cable, R. M. Moon, W. C. Koehler, and E. O. Wollan, Phys. Rev. Lett. **12**, 553 (1964).
[43] T. Kasuya, Prog. Theor. Phys. **16**, 45 (1956).
[44] R. R. Gimaev, A. S. Komlev, A. S. Davydov, B. B. Kovalev, and V. I. Zverev, Crystals **11**, 82 (2021).
[45] E. Plekhanov, P. Hasnip, V. Sacksteder, M. Probert, S. J. Clark, K. Refson, and C. Weber, Phys. Rev. B **98**, 075129 (2018).
[46] E. Plekhanov, N. Bonini, and C. Weber, Phys. Rev. B **104**, 235131 (2021).
[47] N. Tateiwa, A. Nakagawa, K. Fujio, T. Kawae, and K. Takeda, Phys. B: Condens. Matter **359-361**, 142 (2005).
[48] J. Song, W. Bi, D. Haskel, and J. S. Schilling, Phys. Rev. B **95**, 205138 (2017).
[49] J. J. Hamlin, J. R. Jeffries, G. Samudrala, Y. K. Vohra, S. T. Weir, D. A. Zocco, and M. B. Maple, Phys. Rev. B **84**, 033101 (2011).
[50] R. J. Husband, I. Loa, G. W. Stinton, S. R. Evans, G. J. Ackland, and M. I. McMahon, Phys. Rev. Lett. **109**, 095503 (2012).
[51] R. J. Husband, I. Loa, K. A. Munro, E. E. McBride, S. R. Evans, H.-P. Liermann, and M. I. McMahon, Phys. Rev. B **90**, 214105 (2014).